Linear and nonlinear optical properties of the langasite crystal Ca3TaAl3Si2O14

Théodore Remark, Patricia Segonds, Jérôme Debray, David Jegouso, Encarnación G Víllora, Kiyoshi Shimamura, Benoît Boulanger

Research Article | Vol. 13, No. 7 / 1 Jul 2023 / Optical Materials Express 2053
Optical Materials EXPRESS

Linear and nonlinear optical properties of the langasite crystal $Ca_3TaAl_3Si_2O_{14}$

THÉODORE REMARK,[1] PATRICIA SEGONDS,[1,3] JÉRÔME DEBRAY,[1] DAVID JEGOUSO,[1] ENCARNACIÓN G. VÍLLORA,[2] KIYOSHI SHIMAMURA,[2] AND BENOÎT BOULANGER[1,4]

[1]*Univ. Grenoble Alpes, CNRS, Grenoble INP, Institut Néel, F-38000 Grenoble, France*
[2]*Research Center for Electronic and Optical Materials, National Institute for Materials Science (NIMS) 1-1 Namiki, Tsukuba, 305-0044, Japan*
[3]*patricia.segonds@neel.cnrs.fr*
[4]*benoit.boulanger@neel.cnrs.fr*

Abstract: We have shown that the optical sign of the uniaxial langasite crystal $Ca_3TaAl_3Si_2O_{14}$ is positive. We also measured the phase-matching conditions of second-harmonic generation and sum-frequency generation up to 3.5 µm. Simultaneous fitting of these experimental data allowed us to report the Sellmeier equations of the ordinary and extraordinary principal refractive indices, and the magnitude of the nonlinear coefficient.

1. Introduction

Crystals from the large Langasite family with the general formula $A_3BC_3D_2O_{14}$ have been widely studied for their remarkable high temperature piezoelectric properties [1,2]. These crystals belong to the *32* trigonal point group. The orientation of the dielectric frame (*x, y, z*) with respect to the crystallographic frame (*a, b, c*) is fixed and identical in all these crystals: the *c*- axis corresponds to the *z*-axis and it is perpendicular to the *a*- and *b*-axes forming an angle (*a, b*) = 120°, the *a*-axis being along the *x*- axis and (*y, b*) = 30° since the *y*-axis is perpendicular to the *x*-axis. These crystals can also exhibit second-order nonlinear optical properties since they belong to an acentric point group. Three of them have been studied in this context: $La_3Ga_{5.5}Ta_{0.5}O_{14}$ (LGT) [3], $La_3Ga_{5.5}Nb_{0.5}O_{14}$ (LGN) [4,5] and $La_3Ga_5SiO_{14}$ (LGS). The second-order electric susceptibility tensor $d^{(2)}$ has four non-zero coefficients linked by: $d_{xxx} = - d_{xyy} = - d_{yxy} = - d_{yyx}$ under Kleinmann assumption ; it is called d_{11} in the contracted notation. As all Langasite crystals are trigonal, they belong to the uniaxial optical class. They therefore have two principal refractive indices, *i.e.* n_o and n_e where *o* and *e* stand for "ordinary" and "extraordinary" respectively. LGT, LGN and LGS have all been reported as positive uniaxial crystals ($n_o < n_e$), but only LGT and LGN have provided birefringence phase-matching (BPM) conditions [3,4,5,6]: the measured data have been used to refine their Sellmeier equations describing the normal dispersion of their principal refractive indices, on the one hand, and to determine the magnitude of d_{11}, on the other.

In this paper, we have carried out the first linear and nonlinear optical properties of another Langasite crystal, *i.e.* $Ca_3TaAl_3Si_2O_{14}$ (CTAS), also known for its good piezoelectric properties [7,8]. We recorded its transparency range in polarized light and showed that its optical sign is positive. We also measured the BPM angles and conversion efficiencies of second-harmonic generation (SHG) and sum-frequency generation (SFG) up to 3.5 µm, and determined the Sellmeier equations of n_o and n_e as well as the magnitude of d_{11}. Finally, we estimated the optical damage threshold.

#496056 https://doi.org/10.1364/OME.496056
Journal © 2023 Received 22 May 2023; revised 12 Jun 2023; accepted 12 Jun 2023; published 21 Jun 2023

Optical Materials EXPRESS

2. Determination of the transmission spectrum and optical sign

CTAS crystals were successfully grown using the Czochralski method and were colourless when it was done under appropriate conditions [7,8]. Their congruence allowed the growth of several inches size crystals with a very good optical quality as shown in Fig. 1. All the measurements performed in the present paper used samples cut in the same bulk crystal.

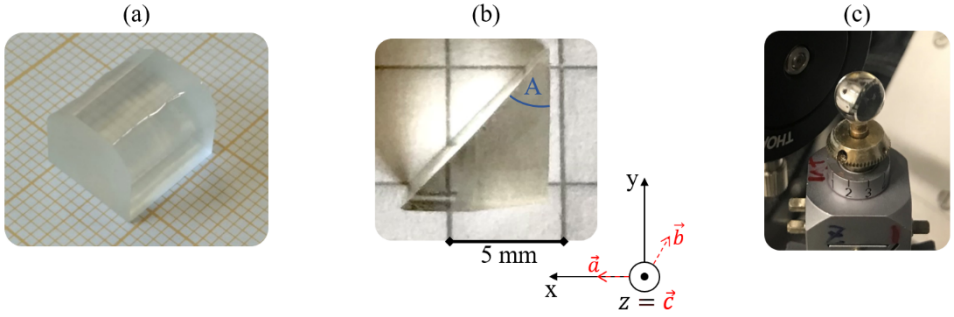

Fig. 1. (a) Bulk CTAS crystal grown by the Czochralski method, (b) CTAS oriented prism for the determination of the refractive indices, (c) CTAS sphere for the phase-matching measurements.

We recorded the transmission spectra of CTAS in polarized light by combining two commercial spectrometers: a Perkin-Elmer Lambda 900 working between 0.175 µm and 3 µm, and a Bruker FT-IR spectrometer that we used between 3 µm and 7 µm. In the former, the linear polarization of light was provided by a Glan-Taylor Polarizer that can be rotated perpendicular to the beam. For the second spectrometer, a rotating grid Polarizer had to be used. A 0.53 *mm* thick slab was shaped with two parallel faces of 0.5 cm by 1 cm. Both faces were oriented perpendicular to the y-axis, polished to optical quality but uncoated, as shown in the inset of Fig. 2. Since CTAS is a uniaxial crystal, the ordinary transmission was recorded with the linear polarization parallel to the x-axis; for the extraordinary transmission, the polarization was parallel to the z-axis. The ordinary and extraordinary recorded spectra are depicted in Fig. 2 without the Fresnel corrections.

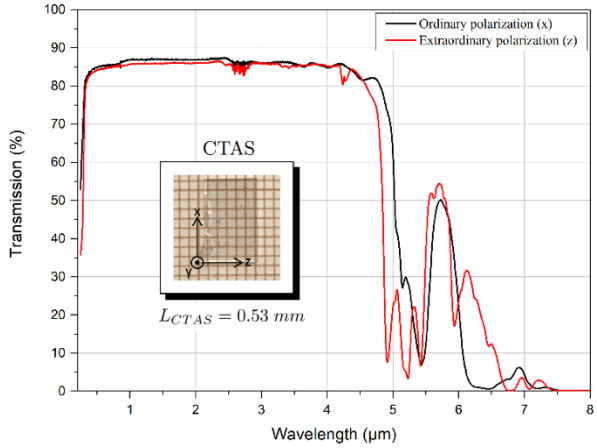

Fig. 2. Transmission spectra recorded in polarized light as a function of wavelength through a 0.53-mm-thick *y*-cut CTAS uncoated slab. The inset shows the crystal sample used for measurements.

Optical Materials EXPRESS

Figure 2 clearly shows that the transmission of CTAS is almost independent of polarization and close to 85% in the visible and infrared below 4.5 µm. At longer wavelengths, it falls to 5% at 5.5 µm and then rises to 50% around 5.7 µm. The transmission falls to zero around 6.5 µm when it is ordinary but above 6.8 µm when it is extraordinary. CTAS can therefore be considered transparent between 0.25 µm and 6 µm which corroborates the results of [7] where a 1-mm-thick slab was used. Further spectroscopic studies will be required to determine the origin of the ultra-violet (UV) and Infra-red (IR) cut-offs.

The prism method was used to determine the magnitude of the two principal refractive indices n_o and n_e of CTAS at the HeNe wavelength $\lambda = 0.6328$ µm, and then the resulting optical sign. The prism was shaped with 5 mm x 5 mm entrance and exit faces forming an angle $A = 46°27'$. Figure 1(b) shows a top view of the prism with the corresponding orientation of the crystallographic and dielectric frames. Both optical faces have been polished and uncoated. Using polychromatic X-rays diffraction in backscattered Laue geometry, the accuracy of all orientations is ± 0.5°. The center of the entrance face of the prism was positioned at the center of the rotating plate of a commercial goniometer, graduated over 360° with an angular accuracy of 1′. It was then possible to access to any direction in the *xy*-plane of CTAS. The beam deflected at the exit of the prism was tracked using a linear CCD array Caliens camera with 2048 pixels of a width of 14 µm. The camera was fixed on the mobile arm of the goniometer used for the observation in order to follow the position of the deflected beam and measure the corresponding deflection angle with the graduation. This angle between the incoming and outgoing beams of the prism, denoted by D, is expected to decrease and then increase when the prism is continuously rotated with respect to the normal incidence on the entrance face. A principal refractive index of CTAS is then determined when D reaches a minimum value, *i.e.* D_m, using the well known equation $n(\lambda) = sin\frac{D_m(\lambda)+A}{2}\left[sin\frac{A}{2}\right]^{-1}$ [9] : by orienting the linear polarization of the HeNe beam parallel to the z-axis, the excited refractive index is n_e, and with the linear polarization perpendicular to the z-axis, it is n_o, which led to the minimum deflection angles D_m equal to 38°20′ and 35°52′ respectively. Then it comes $n_e = 1.7097 \pm 0.0006$ and $n_o = 1.6690 \pm 0.0006$. This measurement shows that $n_o < n_e$, so that the optical sign of CTAS is positive.

3. Birefringence phase-matching angles and Sellmeier equations

We used the sphere method already validated for many studies [10] to measure the BPM directions of CTAS. A sphere of the crystal was shaped with a diameter $D = 8.45$ mm and an acylindricity accuracy $\Delta D/D$ of about 1%. It was polished to optical quality and stuck on the top of a goniometric head that is shown in Fig. 1(c). The CTAS sphere was stuck oriented along the x-axis with an accuracy of ± 0.5° using polychromatic X-rays diffraction in backscattered Laue geometry. Thus, when mounted at the center of an automatic Kappa circle, all directions of the dielectric yz-plane were accessible by using a horizontal rotation stage. The spherical coordinates corresponding to $\varphi = 90°$ and $0° \leq \theta \leq 90°$ could be read directly on the graduation, $\theta = 0°$ corresponding to the z-axis and $\theta = 90°$ to the y-axis. In this plane, Type I SFG($1/\lambda_1^e + 1/\lambda_2^e = 1/\lambda_3^o$) and Type I SHG ($1/\lambda_\omega^e + 1/\lambda_\omega^e = 1/\lambda_{2\omega}^o$) BPM conditions are allowed with a non-zero effective coefficient: the exponents o and e stand for the ordinary and extraordinary polarizations respectively, and $\lambda_1 \geq \lambda_2 > \lambda_3$. The corresponding effective coefficients are written [11]:

$$d_{eff}^{SFG}(\theta_{PM}, \lambda_3^0) = d_{11}(\lambda_3^0)cos[\theta_{PM} - \rho^e(\lambda_1^e, \theta_{PM})]cos[\theta_{PM} - \rho^e(\lambda_2^e, \theta_{PM})] \quad (1)$$

$$d_{eff}^{SHG}(\theta_{PM}, \lambda_{2\omega}^0) = d_{11}(\lambda_{2\omega}^o)cos^2[\theta_{PM} - \rho^e(\lambda_\omega, \theta_{PM})] \quad (2)$$

where $\rho^e(\lambda_i^e, \theta_{PM})$, with the subscript i = 1, 2 or ω, stand for the spatial walk-off angles at the phase-matching angle θ_{PM}.

Optical Materials EXPRESS

For SHG, the incoming beam was emitted by Light Conversion optical parametric source of 15 ps pulse width (FWHM) and 10 Hz repetition rate, tunable between 0.4 μm and 12 μm. For SFG, one of the two beams was emitted by a 10 ns pulse width (FWHM) and 10 Hz repetition rate Continuum Optical Parametric Oscillator (OPO) tunable between 0.4 μm and 2.2 μm, with the second beam being at 1.064 μm. Half-wave plates were inserted into each beam to independently control the orientation of their linear polarization. A 100-mm-focal length CaF_2 lens was placed at an appropriate distance from the entrance face of the sphere to ensure normal incidence and quasi-parallel propagation of all incoming beams along its diameter. This alignment was satisfactory when these conditions were maintained as the sphere was rotated. Low-Pass Filters and a Glan-Polarizer removed all incoming beams from the generated one after the sphere. The wavelengths λ^e_ω for Type I SHG, λ^e_1 and $\lambda^e_2 = 1.064\ \mu m$ for Type I SFG were controlled between 0.4 μm and 1.1 μm with an accuracy of ± 1 nm using a 650 Red Tide IDIL spectrometer, and between 1.1 μm and 1.7 μm with an accuracy of ± 3 nm using a NIRquest 512 Ocean Optics spectrometer. The value of longer wavelengths was determined by measuring the BPM generated wavelengths, *i.e.* $\lambda^o_{2\omega} = \lambda^e_\omega/2$ for Type I SHG, by using the energy conservation $1/\lambda^o_3 = 1/\lambda^e_1 + 1/\lambda^e_2$ after measuring λ^o_3 in the case of Type I SFG. The BPM angles, θ_{PM}, were read directly on the Kappa circle with an accuracy of ± 0.5°. They correspond to a maximum value of the frequency conversion efficiency. A Hamamatsu amplified photodiode S2281-01 was used to record SHG or SFG energies generated below 1.1 μm. It was a Vigo infrared photoelectromagnetic detector (PEM) between 1.1 μm and 4 μm. The incident energies were measured with an OPHIR PE10 Joulemeter. We measured the tuning curve of Type I SHG shown in Fig. 3(a) for λ^e_ω ranging between 0.76 and 3.67 μm, and that of Type I SFG depicted in Fig. 3(b) for 0.7 $\mu m < \lambda^e_1 < 2.3\ \mu m$ and $\lambda^e_2 = 1.064\ \mu m$ as the incoming wavelengths.

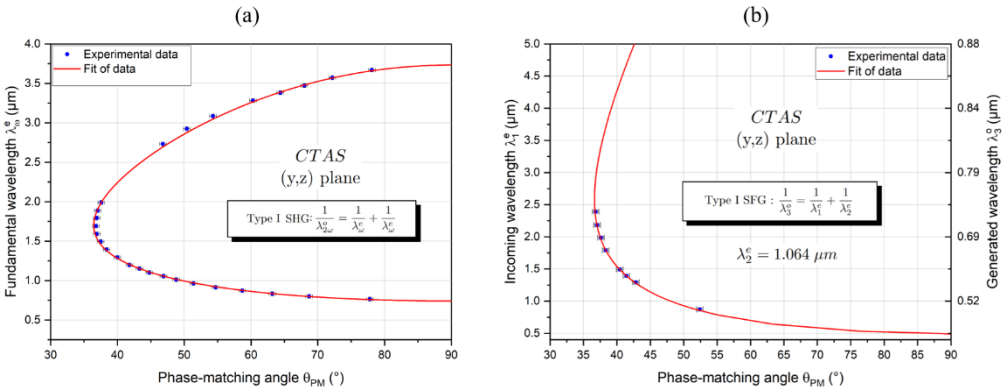

Fig. 3. Type I SHG (a) and SFG (b) tuning curves in the yz-plane of CTAS.

By simultaneously fitting the experimental data of Fig. 3(a) and Fig. 3(b) by a Levenberg-Marquardt algorithm combined with the absolute magnitudes of n_o and n_e at 0.6328 μm given above in section 2, we were able to determine the following dispersion equations of the two principal refractive indices of CTAS with a relative accuracy $\Delta n/n$ of 10^{-4}:

$$n^2_{o,e}(\lambda) = A_{o,e} + \frac{B_{o,e}}{\lambda^2 - C_{o,e}} - D_{o,e}\lambda^2 \tag{3}$$

The wavelength λ is expressed in micron and the magnitude of A_i, B_i, C_i and D_i are given in Table 1. Note that the coefficient C_i with the subscript $i = o$ or e, is associated with the UV cutoff while D_i stands for an infrared correction. The corresponding fitting curves are shown in Fig. 3.

Optical Materials EXPRESS

Table 1. Dispersion coefficients of the principal refractive indices n_o and n_e of CTAS

Dispersion coefficients	i ≡ o	i ≡ e
A_i	2.7410	2.8530
B_i	0.0185	0.0281
C_i	0.0218	0.0210
D_i	0.0084	0.0099

According to the spectral range of the measured phase-matching angles, Eq. (3) and the coefficients of Table 1 provide an accurate calculation of $n_o(\lambda)$ between 0.38 µm and 1.83 µm, and of $n_e(\lambda)$ between 0.76 µm and 3.66 µm.

4. Nonlinear coefficient and optical damage threshold

We used the magnitude of one nonlinear coefficient of KTP, *i.e.* $d_{24}^{KTP}(\lambda_{2\omega} = 0.66\ \mu m) = 2.37 \pm 0.17\ pm/V$, as a reference for determining the magnitude of the single nonlinear coefficient d_{11} of CTAS. The KTP slab was cut in the (*x, z*) plane at$\theta_{PM}^{KTP} = 58,5°$ for achieving type II BPM SHG ($1/\ \lambda_\omega^e + 1/\ \lambda_\omega^o = 1/\lambda_{2\omega}^o$) [10]. We then cut a CTAS slab at $\theta_{PM}^{CTAS} = 38.5°$ in the yz-plane in order to achieve Type I SHG for a fundamental wavelength equal to $\lambda_\omega = 1.32\ \mu m$.The thickness of both CTAS and KTP slabs was small, i.e. $L_{CTAS} = 0.50\ mm$ and $L_{KTP} = 0.50\ mm$, in order to have a negligible spatial walk-off attenuation. They were polished to optical quality and uncoated. The fundamental wavelength was provided by the tunable beam of the OPO described in section 3 which was focused in each slab successively with the same BK7 converging lens of focal length $f = 100\ mm$. CTAS and KTP slabs were stuck on the same goniometric head so that they could be translated perpendicular to the incoming beam when their BPM SHG conditions were studied. The knife method allowed us to determine that the beam waist *radius* was $w_0 = 160\ \pm 5\ \mu m$ inside the CTAS and KTP samples for wavelengths between 1.3 μm and 1.4 μm. This corresponds to a Rayleigh length of the order of $Z_R = 60 \pm 3\ mm$, which is much larger than the slabs thickness and then ensures a parallel beam propagation inside the crystals. The fundamental energy was measured by an Ophir PE10 Joulemeter and set at the low value of 20 μJ in order to avoid any optical damage in the samples and to perform the SHG in the undepleted pump approximation that was used for the data analysis. The fundamental energy was measured with an OPHIR PE10 Joulemeter. The SHG beam energy was measured with a Hamamatsu S2281-01large area amplified photodiode. By using a Glan Taylor polarizer in front of the detector, the fundamental beam was suppressed but for KTP two low pass filters were also required. It was also necessary to use an optical density $D = 10^{-3}$ for KTP in order to have a SHG energy of the same order of magnitude as for CTAS on the photodiode. To observe BPM conditions, the fundamental energy $\varepsilon(\lambda_\omega, 0)$ at the entrance of each slab and the generated energy $\varepsilon(\lambda_{2\omega},\ L)$ on the photodiode were recorded simultaneously for λ_ω ranging between 1.1 and 1.7 µm by an incremental step of 5-10 nm. We determined the *ratio* $\zeta^i = \frac{\varepsilon_i(\lambda_{2\omega}, L)}{\varepsilon_i^2(\lambda_\omega, 0)}$ normalized to its maximal value, i standing for CTAS and KTP. This *ratio* was considered because it is directly proportional to the square value of the associated effective coefficient given by Eq. (2). It is depicted normalized to its maximal value for CTAS in Fig. 4.

Figure 4 shows that the BPM wavelength is $\lambda_\omega^{CTAS} = 1.36\ \mu m$, which is close to the expected value of $\lambda_\omega^{KTP} = 1.32\ \mu m$. The wavelength acceptance is found at $L_{CTAS}\delta\lambda_\omega^{EXP} = 96.5\ mm.nm$. Figure 4 also shows the very good agreement with the calculation using Eq. (2) and (3), which demonstrates the validity of our dispersion equations. It should be noted that the high value of the spectral acceptance and the rise to the right of the calculation shown in Fig. 4 can be explained

Optical Materials EXPRESS

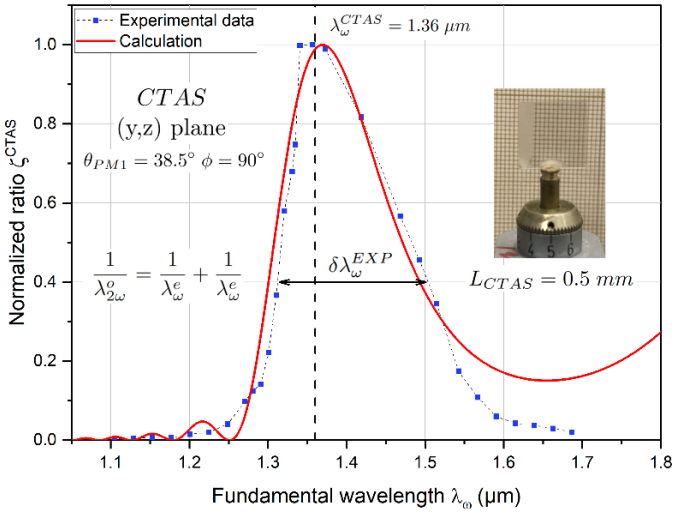

Fig. 4. Measured and calculated normalized ratio ζ^{CTAS} as a function of fundamental wavelength, in the yz-plane of CTAS for Type I SHG. The 0.5 mm-thick slab used is shown in inset.

by the fact that two very close BPM wavelengths are expected for $\theta_{PM}^{CTAS} = 38.5°$ as shown by Fig. 3(a). The comparison between BPM SHG in CTAS and KTP allowed us to express their associated effective coefficients d_{eff}^{CTAS} and d_{eff}^{CTAS} as follows [11]:

$$(d_{eff}^{CTAS})^2 = (d_{eff}^{KTP})^2 \frac{\mathcal{A}^{KTP}}{\mathcal{A}^{CTAS}} \left(\frac{\lambda_\omega^{CTAS}}{\lambda_\omega^{KTP}}\right)^2 \frac{G^{KTP}}{G^{CTAS}} \frac{L_{KTP}^2}{L_{CTAS}^2} \frac{\zeta^{CTAS}}{\zeta^{KTP}} \tag{4}$$

G corresponds to the spatial walk-off attenuation coefficient: $G^{CTAS} = 0.9997$ and $G^{KTP} = 0.9923$. They were calculated from a beam radius of 160 μm and walk-off angles of 1.14° and 2.57° respectively, and crystal lengths of 0.53 mm and 0.50 mm. The coefficients $\mathcal{A}$ are calculated from the Fresnel coefficients and principle refractive indices as in [4]: $\mathcal{A}^{CTAS} = 0.2760$ and $\mathcal{A}^{KTP} = 0.1422$. We found $|d_{11}^{CTAS}(\lambda_{2\omega} = 0.68\ \mu m)| = 0.29 \pm 0.09\ pm/V$. This coefficient is eight times lower than d_{24} of KTP. Applying Miller's rule [12], it comes $|d_{11}^{CTAS}(\lambda_{2\omega} = 0.532\ \mu m)| = 0.30 \pm 0.09\ pm/V$.

The optical damage threshold was investigated under the same conditions at the entrance surface of the previous CTAS and KTP slabs. The protocol was the same as that used previously for the LGT and LGN study [3,4]. The incident beam was provided by a 10-ns pulse duration Nd:YAG Continuum laser at λ=1.064 μm with a repetition rate of 10 Hz. It was focused on the slabs with a lens of focal length f = 200 mm leading to a waist *radius* $w_0 = 64 \pm 5\ \mu m$ measured by the knife method. The corresponding Rayleigh length is $Z_R = 12 \pm 2\ mm$, which is much larger than the thickness of the samples. The incident energy was continuously monitored with the combination of a half-wave plate and a Glan Taylor prism and finally measured over 500 pulses by an OPHIR PE10 Joulemeter. It should be noted that at λ=1.064 μm, both slabs are out of any phase-matching condition according to their orientation. The optical damage threshold was determined from the observation of the early-stage of damage using a CCD camera. The energy was increased by 250 μJ between two successive shots. For CTAS, we found an energy of optical damage threshold $\varepsilon_{Th}^{CTAS} = 3017 \pm 5\mu J$, which corresponds to an intensity of $3.7 \pm 0.6\ GW/cm^2$. It is slightly lower than for KTP for which it comes: $\varepsilon_{Th}^{KTP} = 3751 \pm 5$ μJ, corresponding to an intensity of $4.7 \pm 0.7\ GW/cm^2$.

Optical Materials EXPRESS

5. Conclusion

The linear and nonlinear optical properties of the new $Ca_3TaAl_3Si_2O_{14}$ (CTAS) crystal have been studied for the first time to the best of our knowledge. We measured the transmission spectra in polarized light and the optical damage threshold, and we determined the wavelength dispersion of the two principal refractive indices from direct measurements of BPM conditions. All these data are summarized in Table 2 where they are compared to LGT and LGN which are Langasite crystals also exhibiting nonlinear optical properties. The non-linearity of CTAS is an order of magnitude lower than that of LGT and LGN. Such a difference can be explained once the crystallographic studies have been carried out, such as the measurement of charge density and the relative orientation of the chemical bonds in the unit cell. But CTAS allows SHG to be phase-matched at lower wavelengths, down to ultra-violet, which is a very good feature. The present work also inspires the optical study of CTGAS [13] and SCTAS [14] which belong to the same fully ordered Langasite family. It will also be very interesting to further study in more details $La_3SnGa_5O_{14}$ [15] and Yb:CNGS [16].

Table 2. Comparative table of optical properties of LGT, LGN and CTAS crystals

Crystal	LGT [3]	LGN [4]	CTAS [Present work]
Birefringence $\Delta n = n_e - n_o$ @1.064 µm	0.0251	0.0296	0.0355
Transparency range (µm)	0.3-6.5	0.28-7.4	0.25-6
SHG fundamental wavelength range (µm)	1.3-3.3	1.3-3.6	0.7-3.8
d_{11} (pm/V) @0.532 µm	2.5 ± 0.4	3.0 ± 0.5	0.30 ± 0.09
Intensity damage threshold (GW/cm^2) @1.064 µm – 10 ns – 10 Hz	4.3 ± 0.4	2.8 ± 0.7	3.7 ± 0.6

Disclosures. The authors declare no conflicts of interest.

Data availability. Data underlying the results presented in this paper are not publicly available at this time but may be obtained from the authors upon reasonable request.

References

1. J. Stade, L. Bohatý, M. Hengst, and R. B. Heimann, "Electro-optic, piezoelectric and dielectric properties of Langasite ($La_3Ga_5SiO_{14}$), langanite ($La_3Ga_{5.5}Nb_{0.5}O_{14}$) and langataite ($La_3Ga_{5.5}Ta_{0.5}O_{14}$)," Cryst. Res. Technol. **37**(10), 1113–1120 (2002).
2. J. Bohm, E. Chilla, C. Flannery, H. J. Fröhlich, T. Hauke, R. B. Heimann, M. Hengst, and U. Straube, "Czochralski growth and characterization of piezoelectric single crystals with langasite structure: $La_3Ga_5SiO_{14}$ (LGS), $La_3Ga_{5.5}Nb_{0.5}O_{14}$ (LGN) and $La_3Ga_{5.5}Ta_{0.5}O_{14}$ (LGT) II. Piezoelectric and elastic properties," J. Cryst. Growth **216**(1-4), 293–298 (2000).
3. E. Boursier, P. Segonds, B. Boulanger, C. Félix, J. Debray, D. Jegouso, B. Ménaert, D. Roshchupkin, and I. Shoji, "Phase-matching directions, refined Sellmeier equations, and second-order nonlinear coefficient of the infrared langatate crystal $La_3Ga_{5.5}Ta_{0.5}O_{14}$," Opt. Lett. **39**(13), 4033–4036 (2014).
4. D. Lu, T. Xu, H. Yu, Q. Fu, H. Zhang, P. Segonds, B. Boulanger, X. Zhang, and J. Wang, "Acentric langanite $La_3Ga_{55}Nb_{0.5}O_{14}$ crystal: a new nonlinear crystal for the generation of mid-infrared parametric light," Opt. Express **24**(16), 17603–15 (2016).
5. Y. Wang, F. Liang, J. Wang, D. Lu, H. Yu, and H. Zhang, "Growth of a large-aperture mid-infrared nonlinear optical $La_3Nb_{0.5}Ga_{5.5}O_{14}$ crystal for optical parametric chirped-pulse amplification," CrystEngComm **23**(41), 7212–7218 (2021).
6. Y. Wang, F. Liang, D. Lu, H. Yu, and H. Zhang, "Birefringence dispersion management of Langasite nonlinear crystals for the improvement of mid-infrared amplification," Cryst. Growth Des. **23**(1), 620–628 (2023).
7. X. Fu, E. G. Víllora, Y. Matsushita, Y. Kitanaka, Y. Noguchi, M. Miyayama, K. Shimamura, and N. Ohashi, "Influence of oxygen partial pressure during growth on optical and electrical properties of $Ca_3TaAl_3Si_2O_{14}$ single crystals," Cryst. Growth Des. **16**(4), 2151–2156 (2016).
8. X. Fu, E. G. Víllora, Y. Matsushita, Y. Kitanaka, Y. Noguchi, M. Miyayama, K. Shimamura, and N. Ohashi, "Piezoelectric $Ca_3TaAl_3Si_2O_{14}$ (CTAS): High quality 2-in. single-crystal growth and electro-elastic properties from room to high (650 °C) temperature," J. Cryst. Growth **501**, 38–42 (2018).
9. E. Hecht, "*Optics*," 5 ed. Pearson Education, Inc, Boston, 2017.

Optical Materials EXPRESS

10. B. Boulanger, J. P. Fève, G. Marnier, C. Bonnin, P. Villeval, and J. J. Zondy, "Absolute measurement of quadratic nonlinearities from phase-matched second-harmonic generation in a single KTP crystal cut as a sphere," J. Opt. Soc. Am. B **14**(6), 1380–1386 (1997).
11. B. Boulanger and J. Zyss, "Nonlinear optical properties," in *International Tables for Crystallography* (Wiley, 2006), pp. 178–219.
12. R. C. Miller, "Optical second harmonic generation in piezoelectic crystals," Appl. Phys. Lett. **5**(1), 17–19 (1964).
13. X. Fu, E. G. Víllora, Y. Matsushita, Y. Kitanaka, Y. Noguchi, M. Miyayama, K. Shimamura, and N. Ohashi, "Resistivity and piezoelectric properties of $Ca_3TaGa_{1.5}Al_{1.5}Si_2O_{14}$ single crystals for high temperature sensors," RSC Adv. **7**(89), 56697–56703 (2017).
14. X. Fu, E. G. Víllora, Y. Matsushita, Y. Kitanaka, Y. Noguchi, M. Miyayama, K. Shimamura, and N. Ohashi, "Lattice engineering by Sr-substitution leads to high piezoelectric performance of $(SrxCa1\text{-}x)_3TaAl_3Si_2O_{14}$ single crystals," J. Alloys Compd. **851**, 156860 (2021).
15. H. Lan, F. Liang, X. Jiang, C. Zhang, H. Yu, Z. Lin, H. Zhang, J. Wang, and Y. Wu, "Pushing nonlinear optical oxides into the mid-infrared spectral region beyond 10 μm: design, synthesis, and characterization of $La_3SnGa_5O_{14}$," J. Am. Chem. Soc. **140**(13), 4684–4690 (2018).
16. X. Zhang, Y. Zhou, J. Ren, D. Lu, H. Yu, Z. Wang, S. Guo, and X. Xu, "Growth, thermal and laser properties of a new self-frequency-doubling Yb:CNGS crystal," CrystEngComm **18**(28), 5338–5343 (2016).